The Unsteady Topology of Corner Separations

Ivo Dawkins, James Taylor, Xavier Ottavy, Rob Miller

The Unsteady Topology of Corner Separations

Ivo Dawkins[1]
Whittle Laboratory,
Cambridge CB3 0DY, UK
e-mail: ijrd2@cam.ac.uk

James Taylor
Whittle Laboratory,
Cambridge CB3 0DY, UK
e-mail: jvt24@cam.ac.uk

Xavier Ottavy
LMFA,
Lyon, 69134, France
e-mail: xavier.ottavy@ec-lyon.fr

Rob Miller
Whittle Laboratory,
Cambridge CB3 0DY, UK
e-mail: rjm76@cam.ac.uk

As a compressor is throttled three-dimensional separations develop in the corners between the blades and annulus endwall. Surprisingly, little is understood about the unsteady topology of these separations. One of the problems in studying corner separations is that it is often difficult to understand whether a particular flow structure in the separation is inherent to the separation itself or due to the response of the separation to changes in the inlet flow. In this paper, a novel experimental approach is taken to isolate the corner separation from external influences. A cascade is designed with the specific aim of precisely controlling the inlet flow.

Contrary to earlier work, it is shown that the key saddle and focus pair, which describes the time-mean topology of the corner separation on the endwall, moves smoothly and continuously as the incidence of the flow is raised. This behavior is shown to be the result of the time-resolved topology of the flow field, which comprises numerous saddle and focus pairs that are produced stochastically in regions of high shear strain rate. Most importantly, the separation is shown to exhibit an extremely low-frequency behavior, changing in topology over timescales that are approximately 80 times the convection time through the blade passage. The behavior is shown to be intrinsic to the separation and causes the separation, for periods, to completely disappear from the endwall. This underlying unsteady structure of the separation is shown to have implications for the ability of RANS-based design codes to be able to accurately predict corner separations. [DOI: 10.1115/1.4054676]

Keywords: compressor stall, compressor and turbine aerodynamic design, fluid dynamics and heat transfer phenomena in compressor and turbine components of gas turbine engines

1 Introduction

Understanding the time-averaged topology of three-dimensional corner separations which develop in the corners between the blades and annulus endwall is important in determining the endwall loss and blockage of a blade row. The structure of the time-averaged topology of these separations must also be understood to optimize the three-dimensional geometry of a blade row, as shown by Taylor and Miller [1]. In reality, corner separations are highly unsteady, as demonstrated by Zambonini et al. [2]. Figure 1(*a*) shows the time-averaged topology of a corner separation on a blade operating at a high positive incidence. The separation lines are marked, along with a key saddle/focus critical point pair which bounds the separation line on the endwall. Figure 1(*b*) presents a cross section of the separation near the endwall, showing time-averaged and instantaneous streamlines recorded using particle image velocimetry (PIV) in this study. The shaded region shows the region of axially reversed flow. The saddle and focal points are marked. In the time-averaged flow field, there is one saddle and focus pair, while in the instantaneous flow field there are 15 pairs. It should be noted that only structures larger than 0.4% of the chord can be resolved by the PIV and therefore small-scale turbulent eddies are not resolved. Figure 1 clearly shows the contrast between the unsteady and time-averaged topology of corner separations. This paper aims to precisely measure the unsteady topology of a corner separation and to explain how this defines the time-averaged topology.

A key problem in studying corner separations is that it is often difficult to understand whether a particular flow structure in the separation is inherent to the separation itself or due to the response of the separation to changes in the inlet flow to the blade row. Many previous studies have been in single- or multi-stage compressors. In such environments, the complexities of the spatial and temporal non-uniformities in the inlet velocity and inlet turbulence make studying the cause of flow structures within the separation impossible. Other studies have used linear cascades; however, many of these have attempted to make the inlet flow as representative of a real compressor as possible, using boundary layer trips and boundary layer skew generators. Once again, this added complexity makes studying the cause of flow structures within the corner separation extremely difficult.

In this paper, a different approach is taken. A novel experimental cascade is designed to isolate the corner separation from external influences. In other words, the cascade is designed with the specific aim of precisely controlling the inlet flow to the blade row.

The paper is comprised of seven sections. Section 2 reviews the literature. Section 3 describes the design of the precise cascade experiment. Section 4 describes the time-averaged topology. Section 5 describes the time-resolved topology over time scales up to the convection time through the blade passage. Section 6 describes the time-resolved topology over much longer time scales. Finally, the design implications are discussed in Sec. 7.

2 Corner Separation Topologies

The time-averaged topology shown in Fig. 1(*a*) is one possible arrangement of a corner separation; however, it is not the only known topology. To extend the time-averaged understanding of corner separations to an unsteady understanding, one must first review the different time-averaged topologies that have been documented in the literature.

To describe these topologies, it is necessary to invoke the theory of critical points. First proposed by Poincaré [3], critical point theory describes separated flow topologies in terms of limiting surface streamlines. This was applied by Gbadebo et al. [4] to describe the time-averaged topology of corner separations. Critical point theory stipulates that lines of surface shear stress must obey

[1]Corresponding author.

Contributed by the International Gas Turbine Institute (IGTI) of ASME for publication in the Journal of Turbomachinery. Manuscript received October 6, 2021; final manuscript received January 31, 2022; published online July 4, 2022. Tech. Editor: David G. Bogard.

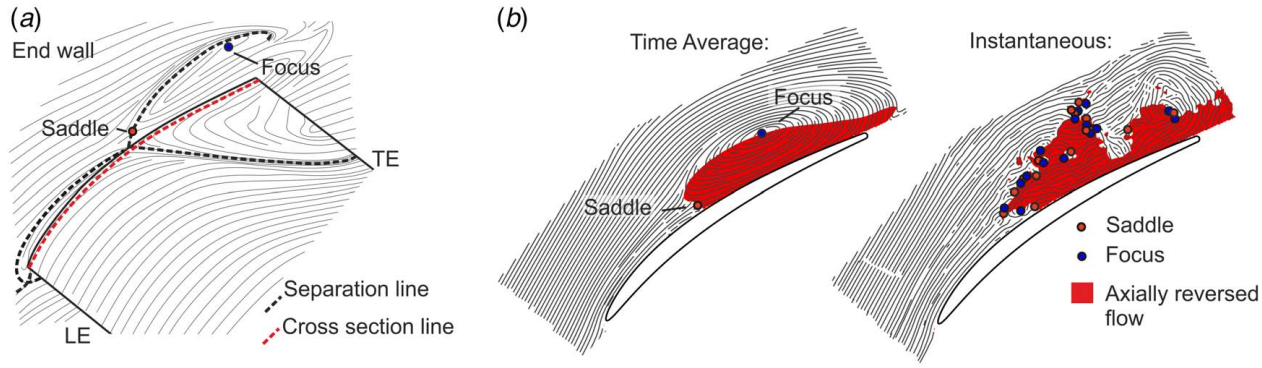

Fig. 1 The time-averaged and unsteady flow topology of a corner separation (design incidence + 4.9°): (*a*) time-averaged skin friction lines showing key saddle/focus pair and (*b*) PIV cross section near-wall spanwise coordinate = 0.008 chord

certain topological rules. A key result of the theory is that separation lines start and end at the shear stress singularities, known as critical points, which are classed as saddles, nodes, and foci. A rigorous definition of these critical point classes is given by Délery [5].

Lei et al. [6] showed that corner separations fit into two topological classes, which are referred to here as "single-sided" and "double-sided". These topologies are shown in Fig. 2, which summarize the characteristic topological features of the classes. In earlier turbomachinery literature, the classes have been referred to as "closed and "open", however, the terms are avoided here as "closed" has a converse meaning in fundamental fluid mechanics, to describe a completely isolated separation with no inflow or outflow.

At low incidence, the topology is referred to as "single-sided" as the separated region is principally confined to the suction surface with little separated flow on the endwall. The separation begins on the endwall upstream of the leading edge (LE) at a saddle point associated with the leading-edge horseshoe vortex. This is marked as point 1 in Fig. 2(*a*). Downstream, the separation line is swept onto the suction surface as the passage boundary layer is overturned onto the blade, where the separation line terminates at a saddle or node on the trailing edge (TE)—out of view in Fig. 2(*a*). As a discontinuity exists at the corner between the endwall and suction surface, the separation line is split by an additional critical point, taking the form of a node on the endwall and saddle on the suction surface—marked as point 2 in Fig. 2(*a*). This point is connected by another separation line to a saddle on the endwall downstream, marked as point 3, causing a very narrow slice of separated flow near the corner. The separated zone on the suction surface may feature several additional critical points, becoming more numerous with increasing incidence, as shown by Gbadebo et al.

At sufficiently high incidence, corner separations bifurcate from the single-sided to double-sided topology, as shown by Taylor and Miller and Lei et al. Double-sided separations are distinguished by a significant region of reversed flow on the endwall which results from the appearance of a saddle and focus joined by a separation line—marked 5 and 6 in Fig. 2(*b*). This leads to the appearance of a new separation surface on the endwall. The simultaneous appearance of the saddle and focus is consistent with the index rule of critical point theory, as given by Délery [5], which states that saddles and nodes or foci are always produced together as pairs. Taylor and Miller identified this key saddle and focus pair as having special significance for aerodynamic performance, causing a large-scale change in the three-dimensional separation structure and consequently an increase in loss and blockage. The focus of this paper is to study the nature of the single-sided to double-sided topology change in the time-resolved flow.

It should be noted that the blade in Fig. 2 does not have a fillet. Details of the topology are different on a filleted blade due to the absence of a sharp discontinuity at the corner. However, the single-sided and double-sided topological definitions still hold, as shown by Taylor and Miller. For completeness, a schematic of these topologies on a filleted blade is given in Appendix A. From this point, the paper will only consider the non-filleted case.

3 Designing a Precise Experiment

It will be shown in this section that as the inlet incidence is raised on a cascade with a uniform inlet velocity, the corner separation which forms has the same structure as the corner separation which results when the inlet flow is representative of a real compressor. This means that it is possible to study corner separations in

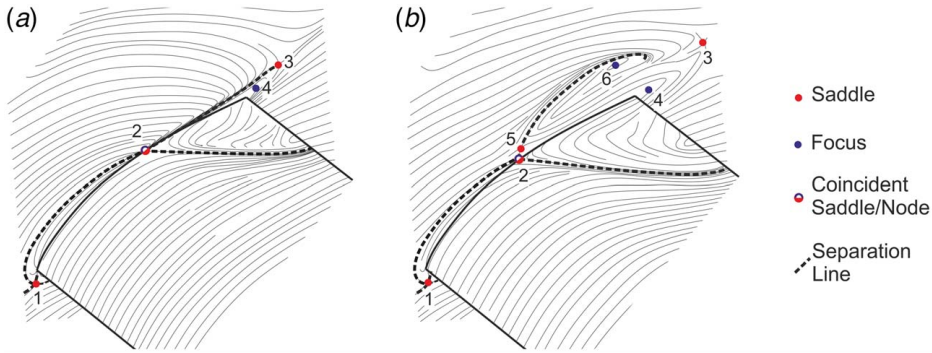

Fig. 2 Characteristic features of the two topological classes of corner separations, on a blade without a fillet. Based on the studies by Gbadebo et al. [4], Lei et al. [6], and Taylor and Miller [1]: (*a*) single-sided topology and (*b*) double-sided topology.

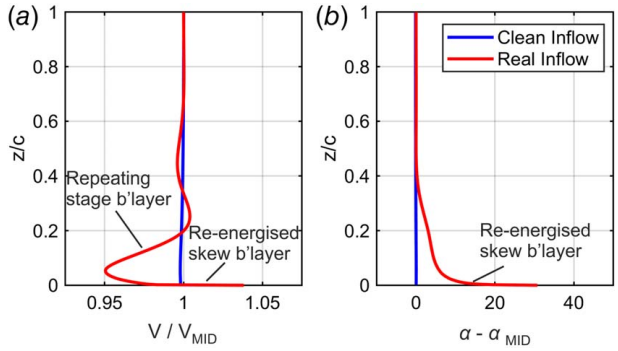

Fig. 3 Features of a "real" multistage stator inflow profile from Auchoybur and Miller [7] versus a "clean" inflow: (*a*) velocity and (*b*) flow angle, relative to midspan

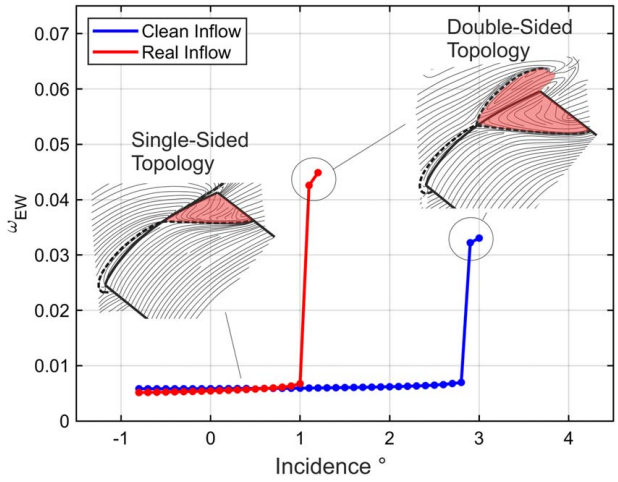

Fig. 4 Endwall loss loops for RANS cascade simulations featuring the "real" and "clean" inlet flow profiles

cascades with uniform inlet flows. This has the advantage that the inlet flow can be set up with a greater degree of precision. The second part of this section will show the design of the controlled cascade experiment. The final part of this section will show the performance of the mid-height section of the blade in terms of transition and loss.

3.1 Simplifying the Inlet Condition. A row of compressor blades embedded in a multistage compressor has an inlet flow which is set up by the integral effect of the upstream compressor stages. An example of such a real inlet condition is shown in Fig. 3. The inlet flow is made up of two parts: the first is what is referred to as the repeating stage boundary layer, which is built up over the upstream stages. The second is the re-energized skew boundary layer which is caused by the frame of reference change between the upstream blade row and the blade row being studied. The complexity of this inlet flow makes it difficult to control in a precise way. In the literature, authors have attempted to reproduce this inlet flow either by testing in a real multistage machine or by building complex inlet flow conditioning systems. In both cases, the attempt to introduce realistic inlet conditions introduces great uncertainty.

To understand the effect of the inlet condition on the topology of the corner separation, a numerical study was undertaken. The study was not intended to precisely model the true topology of corner separations—an experiment or direct numerical simulation would be required for this—but instead to study the sensitivity of the topology to inlet flow conditions.

The computational fluid dynamics (CFD) setup for the study is shown in Table 1. The blade geometry used in the study was a controlled diffusion type designed at the Whittle Laboratory, Cambridge, UK. The inlet flow profiles to the blade row were taken from a study by Auchoybur and Miller [7]. Their study included multistage cantilevered and shrouded compressor configurations. The velocity and flow angle profiles relative to midspan were extracted at the inlet to an embedded blade row. To artificially generate a large number of inlet profiles, the spanwise distributions of velocity and flow angle were linearly scaled to produce several intermediate profiles, between the real inlet profile (the red line in Fig. 3) and a completely clean inflow (the blue line). This was repeated for several of the different configurations studied by Auchoybur and Miller to produce a total of 56 inlet profiles. Using these, 56 numerical simulations were undertaken.

Table 1 RANS setup

Parameter	Value
Turbulence model	$\kappa-\omega$ shear stress transport (SST)
Transition modeling	Fully turbulent
Number of nodes in the mesh	1×10^6
y+	~1
Reynolds number	5×10^5

For brevity, only the loss loops of two of the cases, the inlet flow cases shown in Fig. 3, are shown in Fig. 4. The whole set of results shows a very similar behavior to that reported by Lei et al. [6] and Taylor and Miller [1]. All cases show a sudden topology switch at a critical incidence where the separation becomes unstable and switches from single-sided to double-sided. This is marked by the appearance of a large region of separated flow on the endwall.

From the perspective of the current work the important thing to recognize is that in all cases, no matter what the inlet flow conditions were, the solutions showed the same topological switch. It was also observed that the topology of the corner separation when either single-sided or double-sided was identical for all cases. What changes as the inlet profile varies is the critical incidence at which the topology change occurs. This critical incidence was found to correlate with the integrated momentum deficit of the inlet profile, relative to the momentum at midspan. The highest critical incidence occurred for the clean inlet, where the momentum deficit was zero.

The important point from the perspective of this study is that the topological development of the corner separation is independent of inlet flow conditions, and therefore to achieve the greatest precision in an experiment, a uniform inlet can be used.

3.2 Experimental Configuration. The aim of the experiment is to precisely control the inlet flow to the cascade. This involves precisely controlling the inlet boundary layer, the inlet incidence, and the inlet turbulence. The control of each will be discussed in turn.

The parameters of the cascade are shown in Table 2. The blade profile is a controlled diffusion type designed at the Whittle Laboratory, Cambridge, UK. The experiments were performed in the linear cascade facility at LMFA, Lyon, France. Details of the measurement and post-processing techniques are given in Appendix B. It is intended that this test case will be made public.

3.2.1 Inlet Boundary Layer. To precisely fix the inlet boundary layer, the tunnel boundary layers were bled off at an axial position of 50% of the chord upstream of the blade row, as shown in Fig. 5, and then the growth of the new boundary layer was carefully controlled. The bleed system in Fig. 5 was controlled by an automated exit throttle on the tunnel. This had two benefits. First, it allowed the bleed to be quickly and precisely controlled, and second it isolated the exit of the cascade from the environment.

Table 2 Cascade parameters

Symbol	Name	Value
C	True chord	125 mm
S	Pitch	70.6 mm
H	Span	290 mm
Re	Chord-based Re	3.2×10^5
V_∞	Inlet velocity	39 m/s
α_{DES}	Design inflow angle	52.8 deg
γ	Blade stagger	35.4 deg
χ_{LE}	Inlet metal angle	59.0 deg
χ_{TE}	Outlet metal angle	22.5 deg

To carefully control the growth of the new endwall boundary layer a system of micro pressure tappings, mounted around the bleed lip, is shown in Fig. 6. For each flow condition, the bleed was altered until the stagnation point was located at tapping 4. This meant that at all flow conditions, the pressure profile around the bleed lip was held constant and therefore the inlet boundary layer thickness was consistent between runs.

To confirm this, a hot-wire boundary layer traverse was undertaken at 25% of the chord upstream of the cascade. This was undertaken at two cascade incidences and three evenly spaced locations across a single blade pitch. The results plotted for the design incidence in Fig. 7, show that the boundary layer had a momentum thickness $\theta/c = 0.0020$, with an uncertainty of ±6%, across all flow conditions and the blade pitch. The shape factor of the boundary layer is $H = 1.69 \pm 3\%$.

To check that the bleed system did not introduce any low-frequency unsteadiness to the boundary layer entering the blade row, a 10 Hz low-pass filter was applied to the hotwire measurements and the time-resolved shape factor of the boundary layer was determined. It was found that the boundary layer was effectively time-invariant with a shape factor variation of ±0.02%, within a confidence interval of ±2 standard deviations. The boundary layer profile in the ±2 standard deviation confidence interval is shown in Appendix C.

3.2.2 Incidence. The incidence onto the cascade was determined by measuring the pressure distribution around the mid-height blade profile using 25 tappings and then undertaking the best fit against a database of MISES flow predictions at angle increments of 0.1 deg. MISES is an Euler code with a coupled boundary layer solver, Drela [8]. The pressure distribution around the mid-height of the blade is particularly sensitive to incidence and insensitive to the accuracy of the boundary layer prediction in MISES. The method is therefore extremely accurate, allowing the incidence to be determined to an accuracy of approximately ± 0.1 deg, much better than could be measured by an upstream probe. A comparison

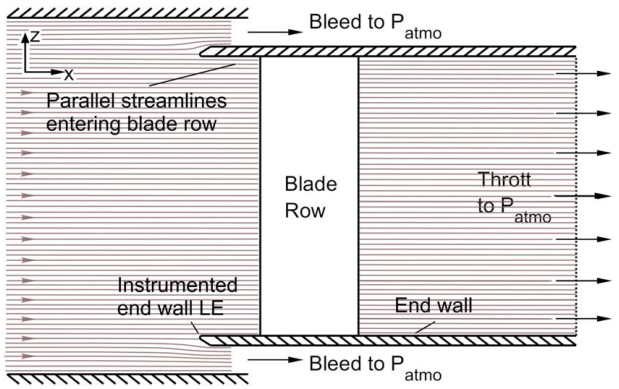

Fig. 5 Cascade configuration to generate uniform inflow, using the throttle-controlled bleed system

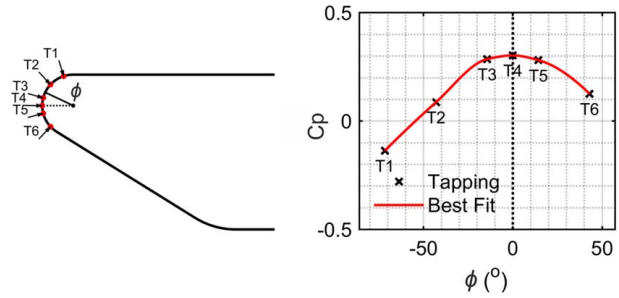

Fig. 6 Bleed lip pressure tappings and Cp distribution, showing balanced operation of the bleed system

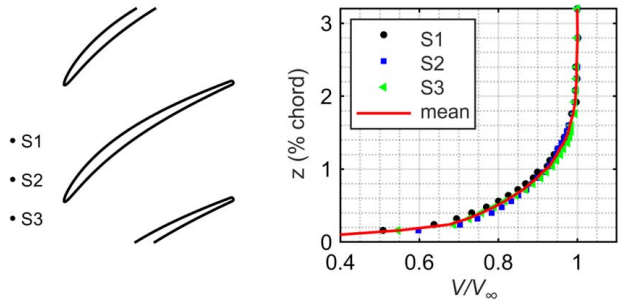

Fig. 7 Inlet boundary layer profile, measured 0.25c upstream of the cascade leading edge at three-pitch locations

of the pressure measurements and best fit MISES solutions is shown in Fig. 8. All incidences presented in this paper are measured relative to the design incidence.

3.2.3 Inflow Turbulence. Freestream turbulence was generated by an upstream grid. The turbulence intensity was measured using a hot-wire positioned 0.25c upstream of the cascade. The intensity was 2.4% with an uncertainty of ±0.1%. The length scale of the turbulence was 2% of the blade chord. The grid was located 280 bar widths upstream of the cascade to ensure the turbulence was isotropic. The grid was present at all operating incidences.

For precision, the long length scale variation of the tunnel velocity was measured by applying a 10 Hz low-pass filter to a two-minute acquisition of freestream hot-wire data. Long length scales were found to result in 0.3% variations of the tunnel inflow velocity in the frequency range below 10 Hz. This shows that the tunnel velocity is effectively time-invariant, with a Reynolds number variation of 0.3%.

3.3 Mid-Height Cascade Performance. As the incidence is changed, it is important to characterize the aerodynamic behavior of the blade profile. Figure 9 shows oil flow visualization over the blade suction surface at mid-height as the incidence is

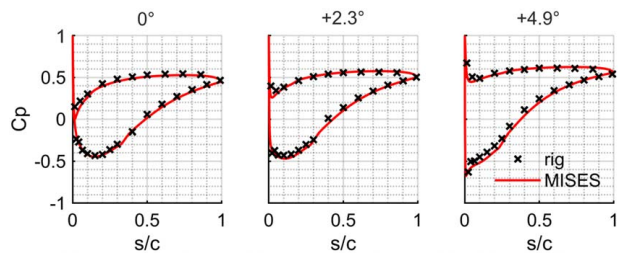

Fig. 8 Mid-height blade Cp distribution at three cascade incidences, with MISES best fit to infer inlet flow angle

changed. It shows that at the design incidence the blade has a small laminar separation bubble at around 35% of the streamwise surface length from the leading edge. As the incidence is raised this can be seen to move forward, reducing in size and finally disappearing at +4.9 deg above design.

A comparison of the transition location and the mid-height mass averaged profile loss measured in the experiment and predicted in MISES is shown in Fig. 10. The prediction of the transition location is correct to within 5% of the surface length and the prediction of profile loss is within 10% of the measured value. Up to +5.5 deg, the difference in profile loss in the adjacent measured blade passages was less than 5% of the average profile loss, indicating good periodicity.

It is important to note that the mid-height boundary layer remains attached at the trailing edge up to +5.5 deg incidence. Above this, a trailing edge separation occurs and moves progressively upstream, raising the profile loss. In this study, the topology of the corner separation is studied at inlet angles of up to +5.5 deg.

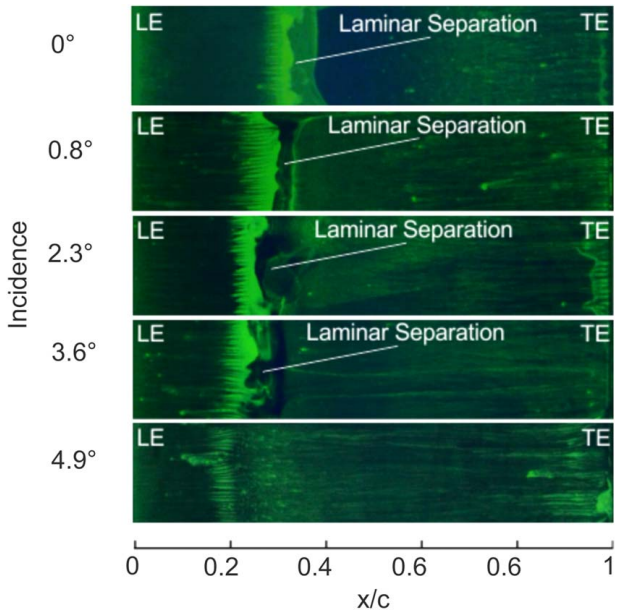

Fig. 9 Mid-height suction surface oil visualization, showing transition via laminar separation at peak suction

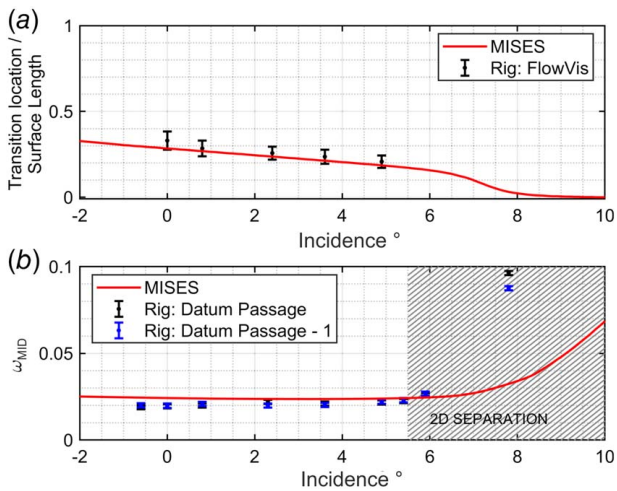

Fig. 10 (*a*) MISES prediction versus measurement of transition location and (*b*) mid-height loss versus incidence

4 Time-Averaged Flow Topology

Contours of loss measured 0.2c downstream of the cascade are shown in Fig. 11. The measurements show a smooth growth in endwall loss as the incidence is raised. At an incidence of +7.8 deg, the blade profile can be seen to be separated at midspan. The time-averaged endwall loss extracted from these measurements is shown plotted against incidence in Fig. 12. The endwall loss is defined as the difference between the mass averaged passage loss and midspan profile loss, as given in Appendix B.

The first thing to note from Fig. 12 is that up to an incidence of +0.8 deg, the endwall loss does not change significantly, and that above +0.8 deg the endwall loss rises smoothly. This is very different from the research findings from the RANS-based studies of Lei et al. [6], and Taylor and Miller [1], which like Fig. 4 show a discontinuity in loss at a critical incidence, as the corner separation changes from single-sided to double-sided. In this section, it will be shown that the smooth rise in loss is due to the time-averaged topology of the corner separation changing smoothly with incidence.

4.1 Endwall Topology. PIV measurements on the spanwise $z/c = 0.008$ plane are shown in Fig. 13. This plane lies within the endwall boundary layer. It should be noted that these measurements show a cross section of the topology very near the endwall, rather than an exact representation of the skin friction lines. The saddles and foci were located using the critical point detection algorithm described in Appendix B, and are marked in Fig. 13. The endwall separation line is also marked. The first thing to note is that, at all incidences, the time-averaged flow field has at most one saddle and focus pair. The second thing to note is that the behavior of this pair is very different from that described in steady computational work in the literature. Using RANS CFD, Taylor and

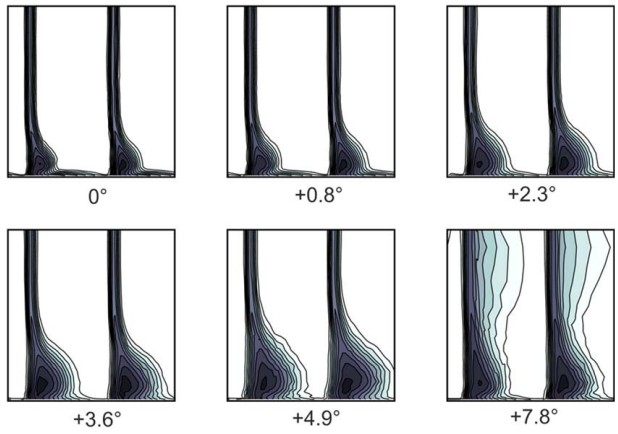

Fig. 11 Contours of total pressure loss coefficient, 0.2c downstream of the cascade at six incidences

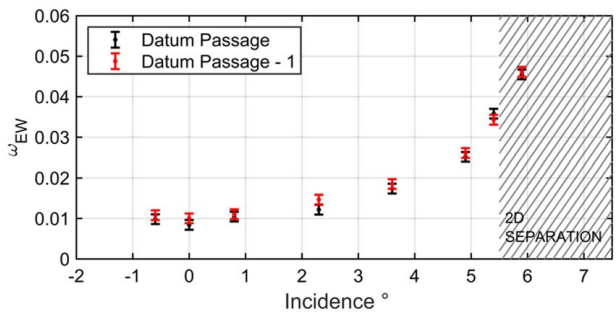

Fig. 12 Development of endwall loss with inflow angle in two adjacent passages

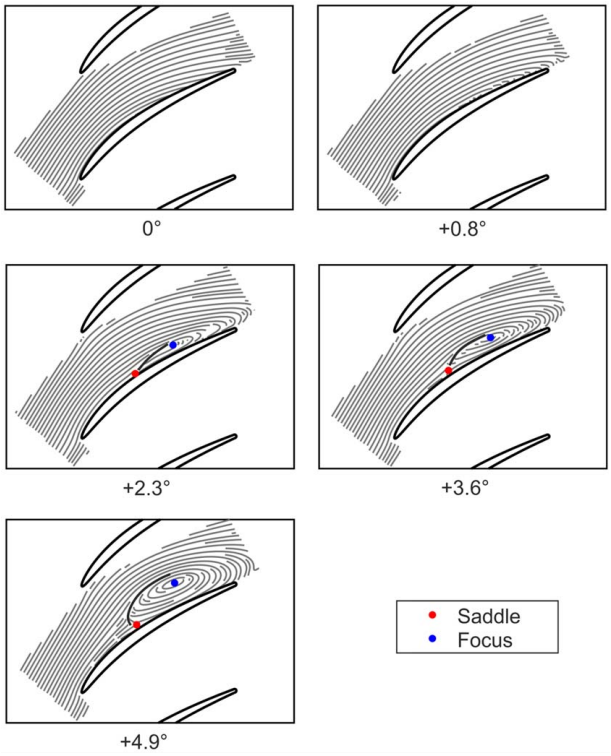

Fig. 13 Time-averaged streamlines and critical point arrangement at z/c = 0.008, measured using high-speed PIV at six incidences. For clarity, the separation line has been cut short in the vicinity of the focus.

Miller [1] showed that a saddle and focus pair emerges at a critical incidence in the blade corner just downstream of peak suction, in the same way as shown in Fig. 13 between +0.8 deg and +2.3 deg incidence. Where the current work differs from Taylor and Miller's findings is in the stability of this pair, once created. In the computation, immediately after the saddle and focus are formed, the focus jumps to a location close to mid-passage while the saddle moves towards the leading edge. This causes an opening of a separation surface between the saddle and focus, resulting in a large rise in loss as the topology of the separation changes from single- to double-sided, in the same way as shown in Fig. 4. This rapid jump in the location of the saddle and focus pair was not observed in the experiment.

In contrast to Taylor and Miller, Fig. 13 shows that the location of the saddle and focus pair remains stable and in the corner. As the incidence onto the cascade is raised, the focus moves smoothly into the passage and the saddle remains in the corner. This causes a smooth rise in the size of the separation surface and a corresponding smooth rise in blockage and loss, as shown in Fig. 12.

Figure 14 shows surface oil flow visualizations of the endwall and suction surface for three incidences, viewed from downstream of the cascade trailing edge. This shows that the separated region on both the endwall and suction surface increases in size as the incidence is raised from 0 deg to +4.9 deg. Figure 15 shows a corresponding view of the time-averaged flow field at $z/c = 0.008$ from the PIV, for the same incidences as shown in Fig. 14. The time-averaged streamlines in Fig. 15 closely resemble the oil flow visualizations in Fig. 14. This confirms that the topology of the velocity field at $z/c = 0.008$ is a close approximation of the skin friction topology on the wall.

4.2 3D Shape of Corner Separation. To measure the three-dimensional shape of the corner separation, a second PIV plane was measured at a spanwise position of $z/c = 0.08$ from the

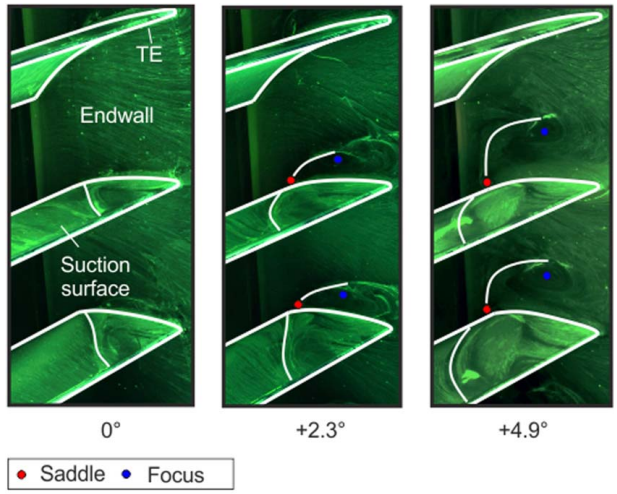

Fig. 14 Oil flow visualization of suction surface and endwall, showing separation line and focus. Viewed from downstream at three incidences.

endwall. This corresponds to the spanwise position of mass averaged peak loss measured 0.2c axially downstream. An example of the time-averaged streamlines on the two PIV planes, at an incidence of +4.9 deg is shown in Fig. 16. Figure 17 shows the development with the incidence of the integrated area of axially reversed flow—the shaded region in Fig. 16—on both planes. It should be noted that the integrated area of axially reversed flow is an inherently 2D parameter; however, it is used here to describe the 3D shape of the corner separation by quantifying the size of the separation cross section at different spanwise locations.

Figure 17 shows that at low incidence, the separation is small near the endwall, with almost no reversed flow on the $z/c = 0.008$ plane at an incidence of 0 deg. A larger cross section of axially reversed flow

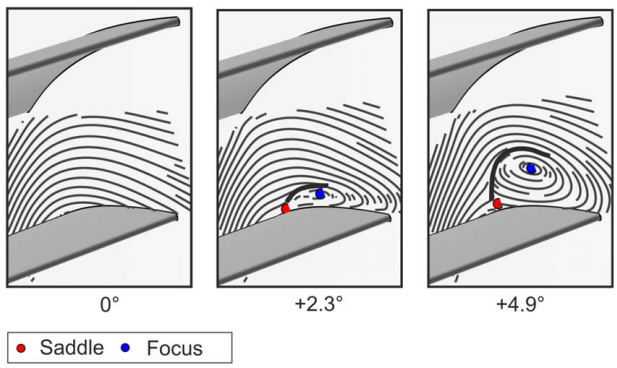

Fig. 15 Time-averaged streamlines from PIV at z/c = 0.008. View angle corresponding to oil flow visualizations in Fig. 14.

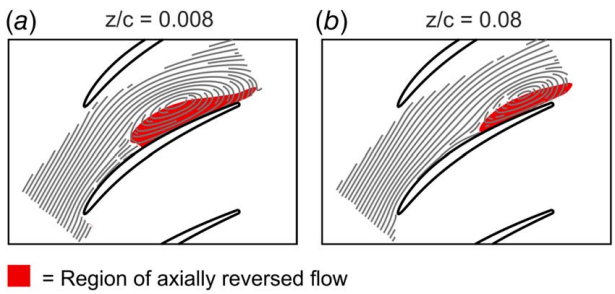

Fig. 16 Cross section of axially reversed flow at two spanwise locations: (a) z/c = 0.008 and (b) z/c = 0.08, at +4.9 deg incidence

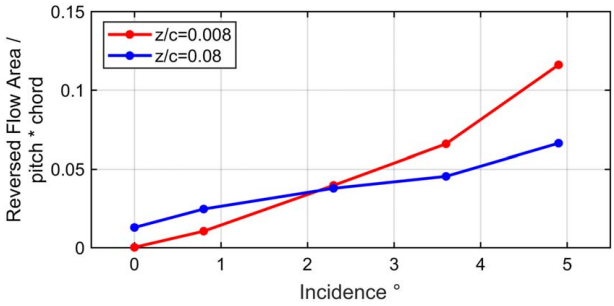

Fig. 17 Development of axially reversed flow cross section with incidence at $z/c = 0.008$ and $z/c = 0.08$

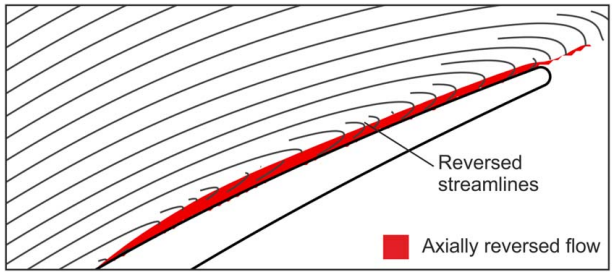

Fig. 18 Axially reversed flow near trailing edge at $z/c = 0.008$ at +0.8 deg incidence, before the first appearance of the saddle/focus pair on the endwall

exists further away from the endwall at $z/c = 0.08$. However, as the incidence is increased, the size of the separation at $z/c = 0.008$ increases at a higher rate than at $z/c = 0.08$. At high incidence, the separation is the largest closest to the endwall, as shown in Fig. 16.

It is interesting to note in Fig. 17 that the region of reversed flow at $z/c = 0.008$ is non-zero at an incidence of +0.8 deg. This incidence is below the point at which the saddle and focus pair have formed. This region of reversed flow is shown in Fig. 18. The region exists close to the suction surface and extends from approximately the position of the two-thirds chord to the trailing edge.

5 Time-Resolved Flow Topology

A time snapshot from the time-resolved PIV at an incidence of +4.9 deg, showing streamlines with saddles and foci, is shown in Fig. 19. This should be contrasted to the time-averaged topology shown in Fig. 13, which is an average of ten thousand snapshots over 1067 throughflows. In the time-averaged flow field, only one saddle and focus pair was present near the endwall, bounding a clearly defined separation line. Figure 19 shows 13 saddle and focus pairs. It should be noted that the spatial resolution of the PIV is 0.4% of chord, and therefore the smallest turbulent eddies are not resolved. The topology is a complex arrangement of streamlines connecting the critical points. This section aims to show where these saddles and foci originate from and how the time-averaged and time-resolved topologies are related.

5.1 Distribution of Critical Points. As the distribution of critical points is stochastic in nature, it is best visualized as a probability density function. This is approximated, in Fig. 20, by cumulatively plotting the locations of critical points for 500 time-steps, over 1067 throughflows. It should be noted that critical points only occur in regions of the flow where the unsteady velocity perturbations are greater in magnitude than the local mean velocity. In practice, this occurs in the region of the separation.

In Fig. 20, at an incidence of 0 deg, a small number of saddles and foci are created in a region close to the suction surface corner. As the incidence is raised to +2.3 deg, the highest density

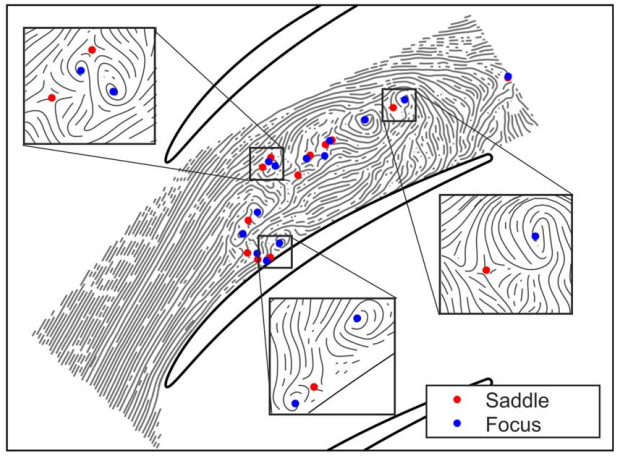

Fig. 19 Instantaneous streamlines and critical point distribution on the $z/c = 0.008$ plane, at +4.9 deg incidence

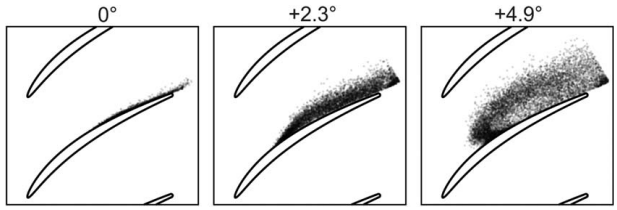

Fig. 20 Cumulative distribution of saddles and foci over 500-time snapshots on the $z/c = 0.008$ plane, for three incidences

of saddles and foci moves to just downstream of peak suction and slightly into the passage away from the corner. These saddles and foci convect downstream and out of the passage. As the incidence rises to +4.9 deg, the region of the highest density of saddles and foci moves further into the passage.

It should be noted that although the number of saddles and foci rises dramatically at higher incidences, saddle and focus pairs are also observed to be created at lower incidence.

5.2 Connection to Shear Strain Rate. The arrangement of focal points in Fig. 20 indicates a concentration of eddy structures on the edge of the separation. This region resembles an unsteady shear layer. To visualize shear regions in the flow, it is informative to examine the distribution of shear strain rate. Here, the in-plane shear strain rate is defined as

$$\varepsilon_{xy} = \frac{\partial u}{\partial y} + \frac{\partial v}{\partial x} \tag{1}$$

In aforementioned equation, u and v are the axial and tangential components of velocity in the PIV plane, and x and y are the axial and tangential coordinates.

Figure 21 shows the distribution of critical points on an instantaneous PIV snapshot at $z/c = 0.008$ and an incidence of +4.9 deg, alongside the magnitude of the in-plane shear strain rate. It is clear that at this time instant, the distribution of critical points closely follows the regions of peak shear strain rate. The right-hand plot of Fig. 21 shows a saddle and focus pair a short time after forming in one of these regions. This is consistent with the findings of Taylor and Miller [1], who showed in a Reynolds-averaged Navier–Stokes (RANS) calculation that the key saddle and focus pair which defines the double-sided topology emerges from a region of very high streamline curvature. In regions of high streamline curvature, the normal velocity gradients on the right-hand side of Eq. (1)

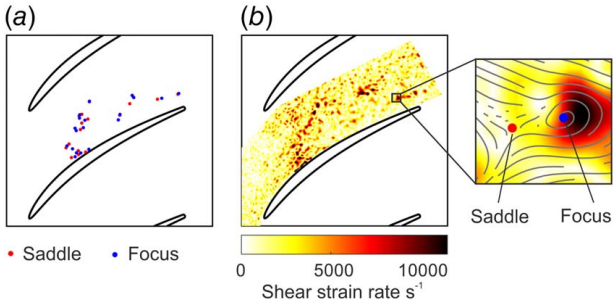

Fig. 21 (*a*) Instantaneous distribution of critical points and (*b*) magnitude of instantaneous in-plane shear strain rate, ε_{xy}. On the $z/c = 0.008$ plane, at +4.9 deg incidence.

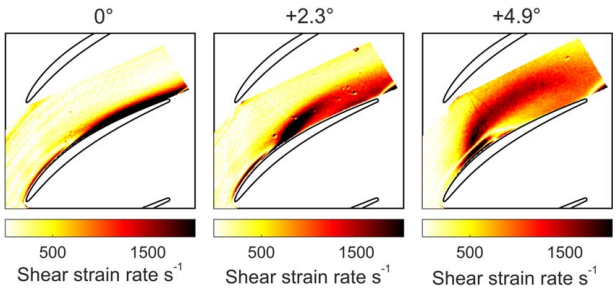

Fig. 22 Magnitude of the mean in-plane shear strain rate, ε_{xy} at $z/c = 0.008$, for three incidences

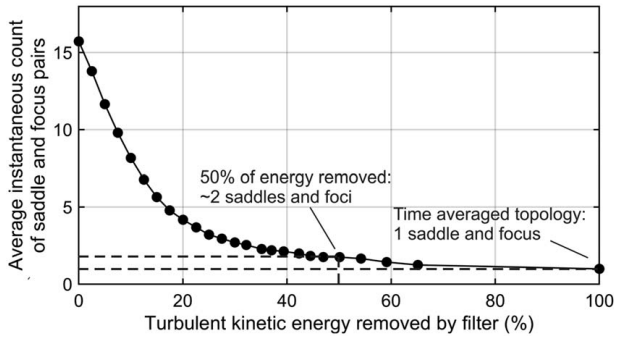

Fig. 23 Cumulative turbulent kinetic energy content plotted against the number of critical points: POD filtering applied to PIV measurements at $z/c = 0.008$, at +4.9 deg incidence

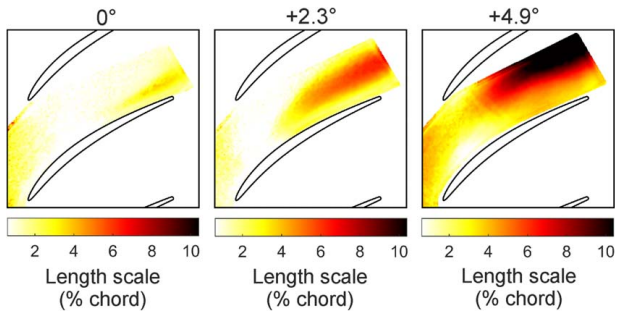

Fig. 24 Spatial integral length scale of unsteadiness on the $z/c = 0.008$ plane, for three incidences

are large. It is therefore expected that saddle and focus pairs should be created in regions coinciding with a locally high shear strain rate.

Figure 22 shows the magnitude of the mean in-plane shear strain rate, averaged over 1067 throughflows. At 0 deg incidence a region of high shear strain rate occurs along the suction side corner, from just downstream of peak suction to the trailing edge. As the incidence is raised to +2.3 deg this region of high shear strain rate becomes concentrated just downstream of peak suction and moves into the passage, away from the corner. As the incidence is further raised to +4.9 deg, the region of peak shear strain rate moves further into the passage.

Comparison of Figs. 20 and 22 shows that the region of peak saddle and focal point density closely overlays the region of peak shear strain rate. The measurements indicate that the saddle and focus pairs are stochastically created in regions where the shear strain rate is high, in the shear layer at the interface between the separated region and the freestream.

5.3 Energy Distribution in the Unsteady Flow. The critical points in the unsteady flow field are associated with unsteady perturbations over a range of length scales. It is important to understand the length scale over which kinetic energy associated with the unsteady flow is distributed. From this point on we will refer to the kinetic energy associated with the unsteady flow as the turbulent kinetic energy.

To establish a relationship between the length scale of turbulent perturbations in the flow and turbulent kinetic energy content, proper orthogonal decomposition (POD) of the unsteady flow field was undertaken. A complete description of the POD technique is given by Kriegseis et al. [9]. The POD was used to filter out a fraction of the total turbulent kinetic energy content. 0% to 100% of the turbulent kinetic energy was removed by reconstructing the flow field from a limited number of modes, progressively discarding the least energetic. At each stage, the average number of the saddle and focus pairs was calculated over 500 snapshots.

The result is shown in Fig. 23, at +4.9 deg incidence on the $z/c = 0.008$ plane. The figure shows that if none of the turbulent kinetic energy is removed, the flow field has on average 16 saddle and focus pairs. As turbulent kinetic energy is filtered out, the number of saddle and focus pairs is reduced. When 50% of the turbulent kinetic energy is removed, the unsteady flow field has on average approximately two saddle and focus pairs. This is double the number in the time-averaged flow field. This implies that around 50% of the turbulent kinetic energy is associated with length scales that are smaller than half of the separation length, while 50% is associated with longer length scales.

5.4 Length Scales of Unsteadiness. The spatial integral length scales of unsteadiness calculated from the PIV on the $z/c = 0.008$ plane are shown in Fig. 24. It should be noted that before calculating these length scales, a high-pass frequency filter was applied to the unsteady velocity measurements at each point on the measurement plane to ensure that temporal variations at a length scale longer than one convection time through the blade passage were removed. Longer temporal length scales will be discussed in Sec. 6.

In Fig. 24, at the design incidence, a peak length scale of 5% of the blade chord occurs close to the trailing edge. As the incidence is increased to +4.9 deg the peak length scale rises to 12% of the blade chord and its location moves upstream and away from the suction surface.

The integral length scale can be interpreted as a time-averaged measure of the radius of the vortical structures on the edge of the separation. Two snapshots of the flow at an incidence of +4.9 deg are shown in Fig. 25. The time between the snapshots is half a convection time through the blade passage. The same vortical structure is labeled in both snapshots. The average integral length scale at the center of the structure in the left and right plots is 7.8% and 11.4% of chord, respectively.

5.5 Connection to Time-Averaged Topology. It is now possible to understand why the smooth growth of the time-averaged separation with incidence, shown in Fig. 12, differs from the

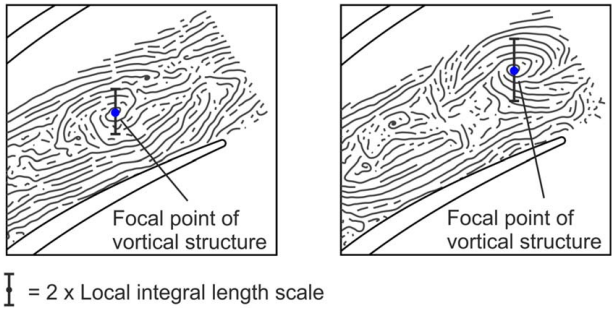

Fig. 25 Vortical structure on $z/c = 0.008$ plane at +4.9 deg incidence, on two snapshots taken half a convection time apart

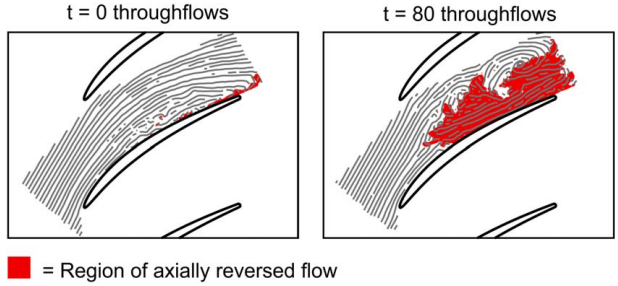

Fig. 26 Instantaneous streamlines and axially reversed flow region at two instances on the $z/c = 0.008$ plane at +4.9 deg incidence

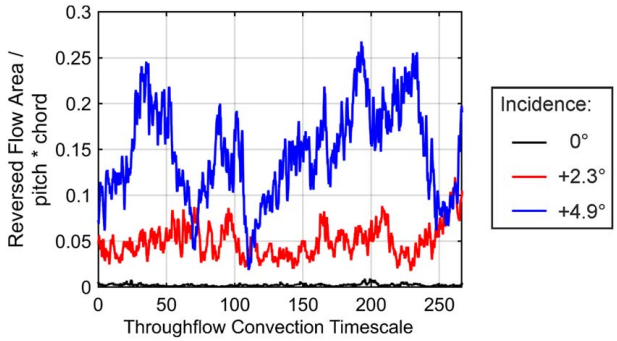

Fig. 27 Time history of axially reversed flow on the $z/c = 0.008$ plane, for three incidences

discontinuous growth presented in numerous RANS studies in the literature.

The first reason is the inherent inaccuracy of RANS codes in modeling corner separations. This is because the unsteadiness in the region of the separation is highly anisotropic. This can be seen in Figs. 24 and 25, where the measurements were made on a plane at 0.8% of chord from the endwall, and the length scale of the vortical structures measured on this plane is up to 12% of the chord in size. This high degree of anisotropy in the unsteady flow, as well as its large length scale relative to the structures in the time-averaged flow field, make it impossible for RANS codes, using the eddy-viscosity hypothesis, to model these flows accurately.

The second reason is the inability of RANS to model the stochastic production of the saddle and focus pairs in the endwall region. In RANS, as the critical incidence is approached, a localized region of very high streamline curvature develops at the junction between the suction surface and endwall. This leads to a locally high shear strain rate. Taylor and Miller [1] showed that it is from this region that the key saddle and focus pair are created, triggering the bifurcation from the single to double-sided topology. In the experiment, as the critical incidence is approached, many localized regions of high shear strain rate occur stochastically resulting in many saddle and focus pairs. It is this stochastic creation of saddle and focus pairs that result in the smooth growth of the time-averaged separation. It is believed that the discontinuous growth of the corner separation that has been observed in RANS-based studies occurs because RANS is unable to model this stochastic behavior.

6 Low-Frequency Topology Change

Large changes in the size of the corner separation were observed over extremely long timescales, at a Strouhal number on the order of 0.01. An example of such a change is shown in Fig. 26, on the $z/c = 0.008$ plane at +4.9 deg incidence. The figure shows the streamlines at two time snapshots, spaced 80 convection times through the passage (0.26 s) apart. It can be seen that the corner separation has changed from being nearly non-existent to filling approximately half the passage.

A time history of the reversed flow area, the shaded area in Fig. 26, is shown in Fig. 27 for three incidences at $z/c = 0.008$. This shows the random nature of the change. Over certain time-periods, the separation takes more than 80 throughflow convection times to drastically change size, shown for example by the ten-fold increase in the reversed flow area between 110 and 190 throughflow times at +4.9 deg incidence. At other times, similar changes can be seen to occur over less than ten throughflow convection times—for example between 100 and 110 throughflow times at +4.9 deg incidence.

Similar low-frequency behavior was observed in a linear cascade experiment by Zambonini et al. [2]. It was believed that the behavior was driven by unsteadiness introduced by the thick endwall boundary layer at the cascade inlet. In the present study, the experiment has been designed to provide a highly controlled inflow, to minimize unsteady perturbations at the inlet as far as possible. This section aims to explain the cause of the low-frequency behavior in this controlled environment.

6.1 Timescale of Low-Frequency Behavior. To obtain a characteristic timescale for the behavior, Kulite unsteady total pressure measurements were taken downstream of the cascade. Figure 28 shows the pitchwise variation in the total power spectrum, 0.2c downstream of the cascade at $z/c = 0.08$. The incidence is +4.9 deg. The spectrum is normalized by the local power at each pitchwise coordinate, to allow a fair comparison of the spectra at the different pitch locations. A dark region of high power is observed in the spectrum downstream of each passage between 1 Hz and 10 Hz. A similar low-frequency region was observed at incidences of 0 deg and +2.3 deg—see Appendix D. The −3 dB bandwidth frequency at the center of the low-frequency region in Fig. 28 is 4 Hz. This corresponds to a characteristic timescale of approximately 80 convection times through the blade passage, or a Strouhal number, $St = fc/V_\infty$, of 0.013.

6.2 Origin of Low-Frequency Behavior. It will be shown in this section that the low-frequency topology change is an intrinsic behavior of the corner separation, as opposed to an artifact of the test rig. This is achieved by showing that the behavior of the separation in any single passage is not induced by low-frequency external perturbations. There are two possible sources of low-frequency external perturbations. The first source is very low-frequency velocity fluctuations in the cascade inlet flow. The second source is a low-frequency blockage transfer between adjacent passages of the cascade, due to a change in blockage in one passage causing a change in incidence onto the adjacent blade.

These sources can be investigated by establishing if the low-frequency behavior is correlated in adjacent passages. If the behavior were driven by inlet perturbations on a time scale of 80 throughflows, it is expected that all passages would be affected

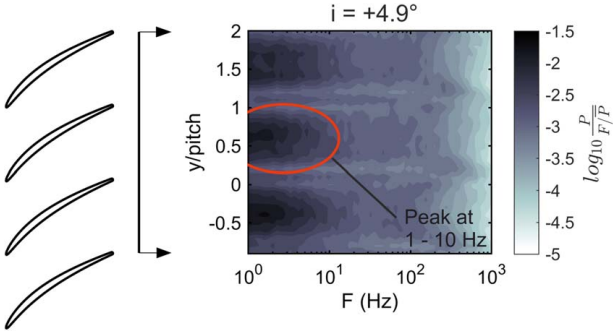

Fig. 28 Pitchwise power spectrum of total pressure normalized by local power, at +4.9 deg incidence. Measured 0.2c downstream of the cascade at $z/c = 0.08$.

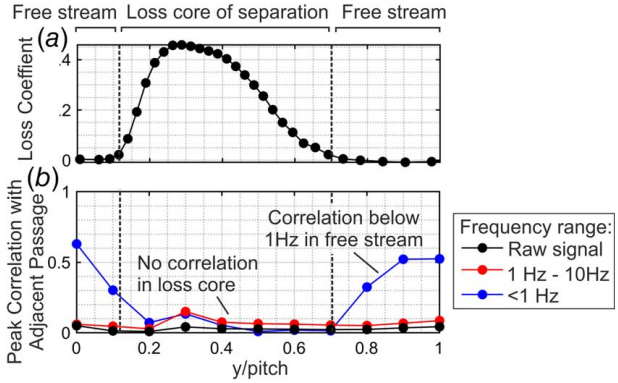

Fig. 30 (*a*) Time-averaged total pressure loss coefficient at $z/c = 0.08$, 0.2c downstream of the cascade at +2.3 deg incidence and (*b*) cross correlation of the unsteady total pressure downstream of adjacent passages, at different pitch locations

simultaneously. If the behavior were due to a disturbance propagating between channels of the cascade, a characteristic time delay would be expected between the low-frequency behavior in adjacent channels. In both cases, a correlation would occur between adjacent channels in the cascade.

To establish if a correlation exists in the cascade, two Kulite unsteady total pressure probes were simultaneously traversed one pitch apart, 0.2c downstream of two adjacent passages at $z/c = 0.08$, as shown in Fig. 29. The peak cross correlations between the signals from the two probes are shown in the bottom plot of Fig. 30, over a range of pitchwise coordinates. The correlation is shown for three different values of the bandpass frequency filter applied to the raw Kulite data. The profile of the total pressure loss coefficient, extracted from the steady total pressure data in Fig. 11, is shown in the top plot to mark the loss core of the corner separation. The black line in the bottom plot shows that over the whole blade pitch, no correlation exists between the unfiltered total pressure signals. When the total pressure signals are filtered to the frequency range of the low-frequency behavior—between 1 Hz and 10 Hz—the signals remain uncorrelated, as shown by the red line. When the total pressure signals are filtered below 1 Hz, a correlation is visible in the freestream, as shown by the blue line. This is the extremely small 0.3% fluctuation of the Reynolds number of the cascade due to the wind-tunnel, identified in Sec. 3.2. However, the correlation drops to zero within the loss core of the separation.

These results show that the low-frequency fluctuations of the corner separations in the neighboring passages are uncorrelated and therefore, that the low-frequency behavior is an intrinsic feature of the separation.

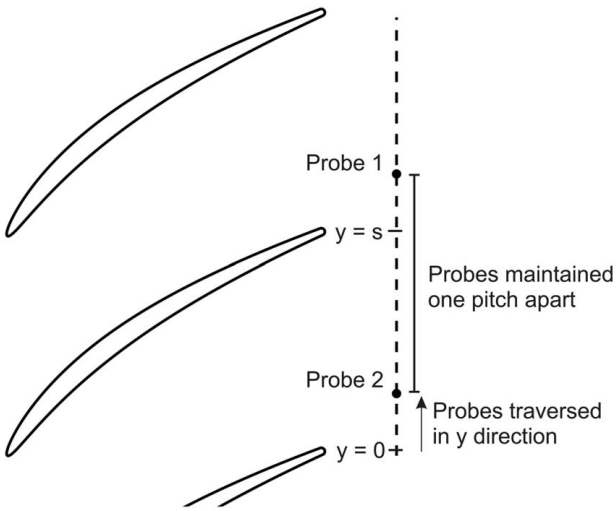

Fig. 29 Configuration of the Kulite total pressure probes, traversed 0.2c axially downstream of two adjacent passages

6.3 Physical Mechanism. The timescale of the low-frequency topology change is significantly longer than the convection timescale in the separated region. At an incidence of +4.9 deg, the timescale of the low-frequency behavior was found to be 25 times longer than the average time for a particle to traverse the reversed flow region in the PIV at $z/c = 0.008$. Therefore, the behavior cannot be explained by a convective phenomenon within the separation.

To understand the mechanism driving the behavior, it should be noted that there is much evidence for similar phenomena in other turbulent separated flow problems. An example in an internal flow was given by Mohammed–Taifour and Weiss, 2016 [10], who studied a wind-tunnel working section with a contoured roof that caused a three-dimensional separation on the opposite wall. The separation was observed to "breathe" at a Strouhal number of 0.01, based on the average separation length and inlet velocity. This resulted in the separation changing in length by up to 90%. Similar dynamics have been observed in external flow problems. Low-frequency lift variations have been widely observed in experiments on stall cells on linear airfoils, at Strouhal numbers between 0.01 and 0.03 based on the airfoil chord and freestream velocity, as shown by Broeren and Bragg [11]. A further example is given by the case of a turbulent wake behind a bluff body at high Reynolds Number. Grandemange et al. [12] showed that a turbulent bluff-body wake exhibits a low-frequency unsteadiness, distinct from periodic vortex shedding, occurring randomly at a Strouhal number of 0.0007 based on the freestream velocity and body height. All three of these problems exhibit large scale, low-frequency dynamics over time scales two to three orders of magnitude longer than the characteristic convection time of the freestream flow.

Progress has been made in recent years in explaining the mechanism for the dynamics of turbulent bluff body wakes through the application of dynamical systems theory. By applying a Langevin model, Rigas et al. [13] and Brackston et al. [14] demonstrated that the low-frequency behavior of bluff body wakes is driven by stochastic turbulent forcing, causing the wake to switch randomly between two opposite asymmetric topologies. In this model, stochastic turbulent perturbations enable the flow to overcome an energy barrier between these two bistable states, resulting in random switching between the two. The behavior occurs at a lower frequency than the stochastic turbulent forcing, as the switching is only triggered by turbulent perturbations that are sufficiently energetic.

In the present study, it was shown in Sec. 5 that large turbulent structures are present on the edge of the separation. It is believed that the stochastic nature of this unsteadiness drives a random,

large-scale change of the topology over very long-time scales, through a mechanism similar to the low-frequency dynamics of turbulent bluff body wakes. However, it should be noted that the structure of the corner separation is significantly more complex than that of a bluff body wake. While the unsteady dynamics of bluff body wakes can be modeled in a two-dimensional or axisymmetric manner, the mechanism for the behavior recorded in this study is likely to be three-dimensional in nature.

7 Design Implications

This work opens up several questions that have implications for compressor design and operation.

First, this study questions the accuracy of RANS codes in the compressor design process. In Sec. 5, it was shown that the unsteady topology of the corner separation is defined by large and highly anisotropic turbulent structures in the shear layer, on length scales of up to 12% of the blade chord. It is impossible for RANS codes, using the eddy-viscosity hypothesis, to be able to model such structures with accuracy. The smooth topological development of the corner separation with incidence, observed in this study, was seen to be very different from the discontinuous growth of the separation that has been presented in numerous RANS-based studies in the literature. This has implications for multistage matching and 3D blade design.

Second, the study may have implications for compressor stability. The low-frequency topology change of the separation was seen to occur at a Strouhal number of 0.013. This corresponds to a departure from the mean flow field on a time scale of approximately one shaft revolution in an engine compressor. It is conceivable that this could influence the stalling behavior of the compressor. This question needs further investigation. Additionally, the low-frequency behavior may have mechanical implications for compressors. The impact of these low frequencies on vibration and aeromechanical modes in an engine is unknown.

Third, it is currently not understood how the low-frequency topology change responds to forcing from unsteady inflow conditions in a real compressor environment. In the multistage environment, the inflow to a blade row contains perturbations over a range of frequencies, most of which are of much higher frequency than the low-frequency behavior. Further investigation is required to understand the impact of these perturbations on the low-frequency topology change.

One final question which must be answered to address these unknowns is how to model the low-frequency behavior. It would be extremely computationally expensive to capture the flow physics in LES. More than 80 throughflows are required to begin to capture the low-frequency behavior. Extrapolating from a recent study by Scillitoe et al. [15], this would currently require approximately one million core hours to model a single blade operating at a Reynolds Number of 2.3×10^5. Practically, this scales to more than 40 days of continuous computation time while running in parallel on 960 cores. Alternative modeling approaches seem to be required. In the literature, progress has been made in applying nonlinear dynamical systems theory to model low-frequency phenomena in much simpler turbulent separated flows—Brackston et al. [14]. It is yet to be seen if similar approaches can be applied to corner separations.

8 Conclusion

This study has identified two scales of unsteadiness in the corner separation. The first scale occurs over relatively short timescales relative to the convection time through the blade passage. This unsteadiness originates from the shear layer on the edge of the separation, where many saddle and focus pairs are created stochastically in regions of locally high shear strain rate. The turbulent structures in the shear layer are large and highly anisotropic, on length scales of up to 12% of the blade chord. These structures define the instantaneous time-resolved topology of the corner separation. The second scale of unsteadiness occurs over much longer timescales, on the order of 80 convection timescales through the blade passage, resulting in a large-scale change in the size of the corner separation. This behavior is shown to be an intrinsic feature of the corner separation and causes the separation, for periods, to completely disappear from the endwall. It is believed that this is due to the separation being stochastically driven to different topological states by the large turbulent structures that exist in the shear layer.

In the resulting time-averaged flow, the key saddle and focus pair, which describes the time-averaged topology on the endwall, moves smoothly and continuously as the incidence onto the cascade is raised. This is in contrast to the discontinuous switch from the single-sided to double-sided topology that is typically observed in RANS codes. It is believed that RANS does not capture the true nature of the topology change due to the highly anisotropic nature of the unsteady flow field and the stochastic creation of saddle and focus pairs in regions of locally high shear strain rate, which RANS is unable to resolve.

These results have implications for the accuracy of RANS codes in the compressor design process, and therefore the optimization of 3D blading and multistage matching. Additionally, the impact of the low-frequency unsteadiness on compressor stability and aeromechanical modes requires further investigation. To address these problems, a wider range of techniques and models are required in the compressor design process, to capture the different scales of unsteadiness exhibited by the separation.

Acknowledgment

The authors would like to thank the Engineering and Physical Sciences Research Council and Rolls-Royce plc for funding and supporting this work. In particular, thanks go to Chris Hall, Harry Simpson, and John Bolger at Rolls-Royce for their time and support. Special thanks go to Nick Cumpsty, for his help in developing the project and interpreting the results. At the Whittle Laboratory, the authors would like to thank Andy Wheeler, Tony Dickens, and Kiran Auchoybur for their many discussions. At LMFA the authors would also like to thank Nathalie Grosjean, Pierre Duquesne, Emmanuel Jondeau, Christoph Brandstetter, Sebastien Goguey, Pierre Laucher, Benoit Paoletti, Gilbert Halter, and Lionel Pierrard for their assistance and advice on conducting the experimental work.

Funding Data

- Engineering and Physical Sciences Research Council (Grant No. RG71341; Funder ID: 10.13039/501100000266).
- Rolls-Royce (Grant No. RG88361; Funder ID: 10.13039/501100000767).

Conflict of Interest

There are no conflicts of interest.

Data Availability Statement

The authors attest that all data for this study are included in the paper. Data provided by a third party listed in Acknowledgment.

Nomenclature

c = true chord
f = frequency
h = blade span
i = incidence
s = blade pitch
u = axial velocity

v = tangential velocity
x = axial coordinate
y = pitchwise coordinate
z = spanwise coordinate
H = boundary layer shape factor
V = velocity
p_{s_∞} = upstream static pressure
p_{t_∞} = upstream total pressure
$p_{t_{out}}$ = downstream total pressure
V_{MID} = inlet velocity at mid-height
V_∞ = upstream velocity
Cp = static pressure coefficient
Re = Reynolds number, based on true chord
St = Strouhal number
α = inlet flow angle
α_{MID} = inlet flow angle at mid-height
α_{DES} = design inlet flow angle
γ = blade stagger
ε_{xy} = shear strain rate
θ = boundary layer momentum thickness
χ_{LE} = inlet metal angle
χ_{TE} = outlet metal angle
ω_T = mass averaged total pressure loss coefficient
ω_{MID} = total pressure loss coefficient at mid-height
ω_{EW} = endwall total pressure loss coefficient

Abbreviations

DNS = direct numerical simulation
LE = leading edge
LES = large eddy simulation
RANS = Reynolds averaged Navier–Stokes
TE = trailing edge

Appendix A: Separations on Blades With Fillets

This appendix presents the characteristic features of single- and double-sided corner separations on blades with fillets, as shown by Taylor and Miller [1]. The single-sided topology is shown in Fig. 31. The double-sided topology is shown in Fig. 32. The principal difference between these topologies and the single- and double-sided topologies of the non-filleted case is the absence of a sharp corner at the junction between the suction surface and endwall. Consequently, the filleted case does not feature the coincidence saddle/node pair, marked as point 2 in Fig. 2.

Appendix B: Experimental Techniques

This appendix provides a summary of the experimental techniques, used in this study to characterize the corner separation. Figure 33 summarizes the measurements taken in the cascade.

Boundary Layer Hot Wire Measurements. The endwall boundary layer measurements presented in Sec. 3.2 were taken using a single axis boundary layer hot wire probe at a sample rate of 200 kHz. The probe was traversed in pitchwise increments to a precision of ±0.01 mm. The probe position was zeroed to a precision of ±0.01 mm.

Pneumatic Five-Hole Probe Measurements. The total pressure measurements presented in Sec. 4 were recorded using a pneumatic five-hole probe. The measurements were taken on a grid of 32 points per passage in the pitchwise direction and 25 points in the spanwise direction. The sample points were clustered in regions of high total pressure gradient, with no less than 15 pitchwise points clustered in the blade wake at each spanwise location. The probe was piloted using a stepper motor-driven carriage, allowing for displacements to a precision of ±0.1 mm. The spatial resolution of the measurements was set by the probe head diameter of 1.6 mm.

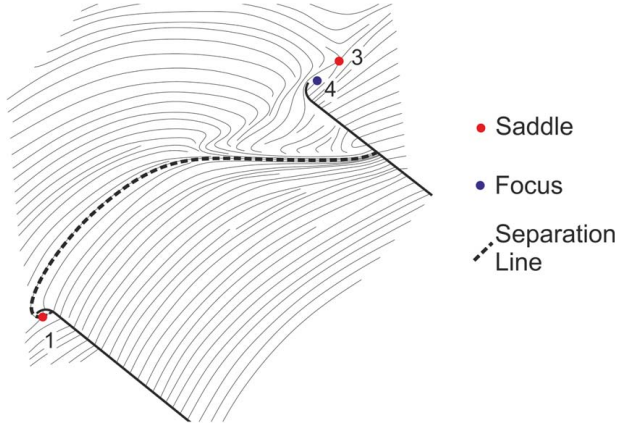

Fig. 31 Topology of a single-sided corner separation on a blade with a fillet. Refer to Taylor and Miller [1].

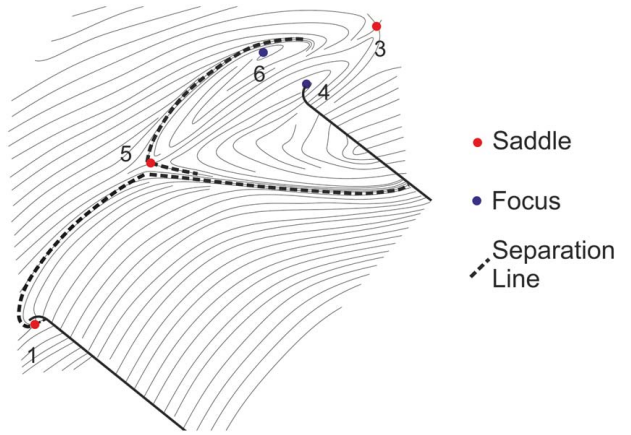

Fig. 32 Topology of a double-sided corner separation on a blade with a fillet. Refer to Taylor and Miller [1].

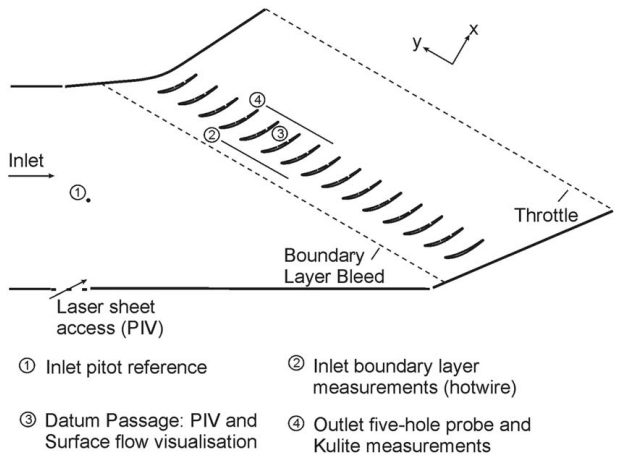

Fig. 33 Side view of cascade showing the location of measurements presented in this paper

Pitot static tubes provided a reference for the total and static pressure at the cascade inlet upstream, to calculate the total pressure loss coefficient

$$\omega = \frac{p_{t_\infty} - p_{t_{out}}}{p_{t_\infty} - p_{s_\infty}} \tag{B1}$$

A mass averaged total pressure loss coefficient was calculated for each passage using the following integration

$$\omega_T = \frac{\int \omega \rho u \, dA}{\int \rho u \, dA} \tag{B2}$$

The mass averaged profile loss was calculated at midspan using the integration

$$\omega_{MID} = \frac{\int_0^s \omega \rho u \, dy}{\int_0^s \rho u \, dy} \tag{B3}$$

The endwall loss was defined as the difference between mass averaged passage loss and profile loss

$$\omega_{EW} = \omega_T - \omega_{MID} \tag{B4}$$

Unsteady Total Pressure Measurements. To obtain the unsteady total pressure measurements presented in Secs. 6.1 and 6.2, Kulite acquisitions were performed on the same downstream sample plane as the five-hole probe measurements to measure the unsteady total pressure field. The measurements were performed using Kulite MIC-093 probes at a sample rate of 100 kHz. The probes were mounted on a non-Kieled probe head and yawed in the mean outlet flow direction to give a measure of the unsteady component of total pressure. The probes were traversed across ten pitchwise positions. All measurements were performed at the spanwise position of $z/c = 0.08$, corresponding to the mass averaged position of peak loss in the pneumatic five-hole probe measurements.

Oil Flow Visualization. The oil flow visualizations presented in Secs. 3.3 and 4.1 were performed using 20cSt silicone oil. Brighter regions of fluorescent oil accumulation indicate low shear stress, and darker regions indicate high shear stress. The surface shear stress vector is shown by the direction of the streak lines.

High-Speed PIV. The high-speed PIV measurements presented in this paper were recorded at 3 kHz over four acquisitions of 0.833 s on each measurement plane. Measurements were performed at two spanwise sample planes from the endwall, of $z/c = 0.008$ (1 mm) and $z/c = 0.08$ (10 mm).

To examine the topological structure of the unsteady flow field, a critical point detection algorithm was employed to extract the location of critical points in the unsteady velocity field. The critical points were located by applying the Newton–Raphson method in two dimensions. Once located, the critical points were classed as saddles, foci, or nodes; based on the local topological arrangement of streamlines. As described by Délery [5], this was achieved by examining the eigenvalues of the Jacobian matrix at the location of the critical point

$$F = \begin{bmatrix} \partial u/\partial x & \partial u/\partial y \\ \partial v/\partial x & \partial v/\partial y \end{bmatrix} \tag{B5}$$

The critical point is identified as a node when both eigenvalues are real and of the same sign. If the eigenvalues are real and of opposite sign, the critical point is a saddle. If the eigenvalues are complex, the critical point is a focus.

Appendix C: Frequencies in Inlet Boundary Layer

The left plot of Fig. 34 shows a power spectrum of velocity, taken from the boundary layer hotwire traverse at a spanwise position of 0.4% chord at the design incidence of the cascade. No significant low frequency components are evident. The right-hand plot of Fig. 34 shows the ±2 standard deviation (2σ) variation in the boundary layer profile, with a 10 Hz low-pass filter applied to the hotwire signal to isolate the low frequency variation of the boundary layer.

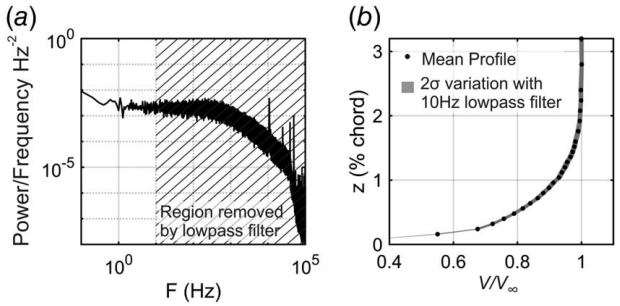

Fig. 34 (*a*) Frequency spectrum at spanwise position of 0.4% of chord, recorded at the design incidence and (*b*) 2σ variation in boundary layer profile below 10 Hz

Appendix D: Downstream Frequency Spectra

Figures 35 and 36 show the same pitchwise power spectra as presented in Sec. 6.1, for cascade incidences of 0 deg and +2.3 deg. At both incidences, a dark region of high power in the spectra is observed between 1 Hz and 10 Hz, as for the case at +4.9 deg incidence presented in Sec. 6.1. This shows that the low-frequency behavior described in Sec. 6 occurs at all incidences of the cascade.

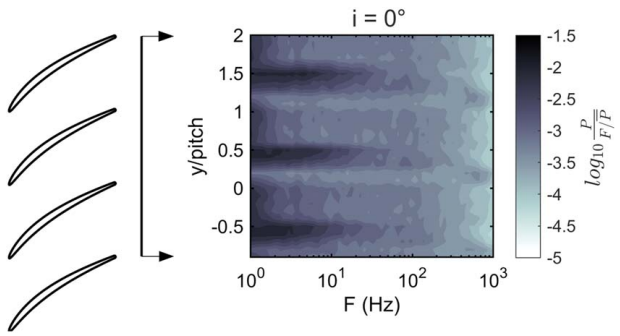

Fig. 35 Pitchwise power spectrum of total pressure normalized by local power at 0 deg incidence. Measured 0.2c downstream at *z/c* = 0.08.

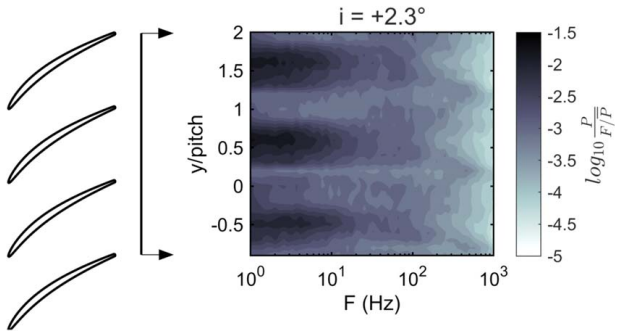

Fig. 36 Pitchwise power spectrum of total pressure normalized by local power at +2.3 deg incidence. Measured 0.2c downstream at *z/c* = 0.08.

References

[1] Taylor, J. V., and Miller, R. J., 2016, "Competing Three-Dimensional Mechanisms in Compressor Flows," ASME J. Turbomach., **139**(2), p. 021009.
[2] Zambonini, G., Ottavy, X., and Kriegseis, J., 2017, "Corner Separation Dynamics in a Linear Compressor Cascade," ASME J. Fluid. Eng., **139**(6), p. 061101.
[3] Poincaré, H., 1891, "Les Points Singuliers Des Equations Differentielles," Compt. Rend. Acad. Science, **1**.

[4] Gbadebo, S. A., Cumpsty, N. A., and Hynes, T. P., 2005, "Three-Dimensional Separations in Axial Compressors," ASME J. Turbomach., **127**(2), pp. 331–339.
[5] Délery, J., 2013, *Three-Dimensional Separated Flow Topology*, Wiley Online Books, ISTE Ltd and John Wiley & Sons Inc, Hoboken, NJ, pp. 1–25.
[6] Lei, V. M., Spakovszky, Z. S., and Greitzer, E. M., 2006, "A Criterion for Axial Compressor Hub-Corner Stall," Proceedings of the ASME Turbo Expo 2006: Power for Land, Sea, and Air, Barcelona, Spain, May 8–11, Vol. 6, pp. 475–486.
[7] Auchoybur, K., and Miller, R. J., 2017, "Design of Compressor Endwall Velocity Triangles," ASME J. Turbomach., **139**(6), p. 061005.
[8] Drela, M., 1986, "Two-Dimensional Transonic Aerodynamic Design and Analysis Using the Euler Equation," Ph.D. dissertation, Massachusetts Institute of Technology, Boston, MA.
[9] Kriegseis, J., Dehler, T., Gnirß, M., and Tropea, C., 2010, "Common-Base Proper Orthogonal Decomposition as a Means of Quantitative Data Comparison," Meas. Sci. Technol., **21**(8), p. 85403.
[10] Mohammed-Taifour, A., and Weiss, J., 2016, "Unsteadiness in a Large Turbulent Separation Bubble," J. Fluid Mech., **799**, pp. 383–412.
[11] Broeren, A., and Bragg, M., 1998, "Low-Frequency Flowfield Unsteadiness During Airfoil Stall and the Influence of Stall Type," 16th AIAA Applied Aerodynamics Conference. Fluid Dynamics and Co-Located Conferences, Albuquerque, NM, June 15–18.
[12] Grandemange, M., Gohlke, M., and Cadot, O., 2013, "Turbulent Wake Past a Three-Dimensional Blunt Body. Part 1. Global Modes and Bi-Stability," J. Fluid Mech., **722**, pp. 51–84.
[13] Rigas, G., Morgans, A. S., Brackston, R. D., and Morrison, J. F., 2015, "Diffusive Dynamics and Stochastic Models of Turbulent Axisymmetric Wakes," J. Fluid Mech., **778**, p. R2.
[14] Brackston, R. D., García de la Cruz, J. M., Wynn, A., Rigas, G., and Morrison, J. F., 2016, "Stochastic Modelling and Feedback Control of Bistability in a Turbulent Bluff Body Wake," J. Fluid Mech., **802**, pp. 726–749.
[15] Scillitoe, A. D., Tucker, P. G., and Adami, P., 2016, "Numerical Investigation of Three-Dimensional Separation in an Axial Flow Compressor: The Influence of Free-Stream Turbulence Intensity and Endwall Boundary Layer State," ASME J. Turbomach., **139**(2), p. 021011.